

Mineralogy and geochemistry of iron tailings from Yeshan iron Deposit,

Southwest Jiangsu, China: Implications for potential utilization

Gang Yang^{1,2}, Quanmin Xie¹, Yidi Li¹, Ranjith Kumar Easwaran⁵, Fang Liu^{3,4,*}, Mei Yang^{2,*}

¹State Key Laboratory of Precision Blasting, Jianghan University, Wuhan, 430056, China

²Faculty of Materials Science and Chemistry, China University of Geosciences (Wuhan), Wuhan 430074, China

³School of Literature, Law and Economics, Wuhan University of Science and Technology, Wuhan 430081, China

⁴Wuhan Explosion and Blasting Co., Ltd., Wuhan, 430056, China

⁵Department of Physics, KPR Institute of Engineering and Technology, Coimbatore 641407, Tamilnadu, India

Corresponding author:

Mei Yang, e-mail, yangmeicug@126.com

Fang Liu, e-mail, francis_liu@live.cn

Abstract

In this work, twenty-one core samples of tailings wastes were collected from Yeshan iron tailings pond in Jiangsu Province, China. The mineralogical-chemical properties of Yeshan iron ore tailings (IOTs) were investigated to explore potential utilization. Mineralogical investigations and mineral liberation analysis indicated that the iron tailings have complex texture and incomplete mineral liberation, suggesting further grinding can improve higher recovery. Yeshan IOTs accumulated much higher MgO originating from dolomite, therefore, it could be infeasible to utilize a large quantity of Yeshan IOTs as alternative raw meals for cement clinker or replace aggregates in concrete. 2D vertical distribution profiles created with the ordinary Kriging method presented heterogeneous distributions of major elements, and the variation trends were inconsistent. The results obtained in this work provide insight for exploiting and reducing Yeshan IOTs.

keywords: tailings wastes; mineralogy; geochemistry; spatial distribution; potential utilization

1. Introduction

The mining industry is a cornerstone of modern society. However, large amounts of mine tailings are deposited on the land surface, cover a vast area, bring environmental pollution problems¹⁻³. In addition, the management of IOTs pond demands for extra time, human resources and money⁴. More seriously, the IOTs dam is a potential safety hazard, threatening people's safety, lives, and property. For instance, in 2019, an IOTs dam collapsed in Brazil caused 235 people death and 35 people missing⁵. The management of IOT is still one of the major social issues worldwide. In China, the reserves of IOTs have reached approximately 5 billion tons, whereas less than 20% of them has been reused^{6, 7}. The "Plan for Preventing and Resolving Safety Risks in Tailings Ponds" jointly issued by eight ministries and commissions in 2020 stipulates that the number of tailings ponds in China will no longer increase, and new "overhead ponds" are strictly forbidden. Iron tailings have gradually become a key factor restricting the sustainable development of mining firms. Therefore, it is urgent to realize great utilization of iron tailings and achieve the purpose of reduction, harmless disposal and recycling treatment.

The application of mineralogical and geochemical characterization to mine waste can contribute to improve risk assessment, guide appropriate mine planning for active mines and optimize remediation design at abandoned mines^{8, 9}. Accordingly, prior to choosing a tailing disposal and management strategy and optimizing an environmental remediation design, it is vital to understand the geochemical and mineralogical properties of tailings¹⁰⁻¹⁴. With these essential and previously research, experiments on utilizing tailings wastes are performed more efficiently and intentionally. These successful studies can be categorized into developing alternative materials for building materials^{15, 16} and ceramics^{17, 18}, and biological reclamation^{19, 20}.

In recent years, minimizing the volume of tailings generated in the original place and maximizing opportunities for alternative uses of tailings have been highly appreciated^{21, 22}. It requires us to have better understanding of geochemical and mineralogical properties of tailings. In this work, we applied an in-situ sampling approach, coupling mineralogical techniques, major element analysis, and visual technology. The properties of iron ore tailings from Yeshan iron deposit were investigated from the perspective of mineralogy and geochemistry to explore the potential utilization, which is beneficial for management to develop robust strategies.

2. Materials and Methods

2. 1 Geology and study area

As shown in Fig. 1, the Yeshan iron tailings pond is located 40 kilometers north of the Nanjing region of Jiangsu Province, China. The Nanjing region has a subtropical monsoon climate with four distinct seasons. The average temperatures in January and July were 2.2 °C and 28.6 °C, respectively²³. The tailings wastes are deposited in a small valley, and the height of the tailings pond is from 78 m to 119 m above sea level. Yeshan iron ore is a hydrothermal metasomatic skarn deposit, thus, the composition of the original iron ore is very complicated. The principal metallic minerals are magnetite and hematite, followed by limonite, pyrite and chalcopyrite. Gangue minerals are mainly serpentine, dolomite and quartz, and small amounts of mica, kaolin, chlorite, etc. The tailings pond deposits more than 6 million cubic meters of iron tailings wastes.

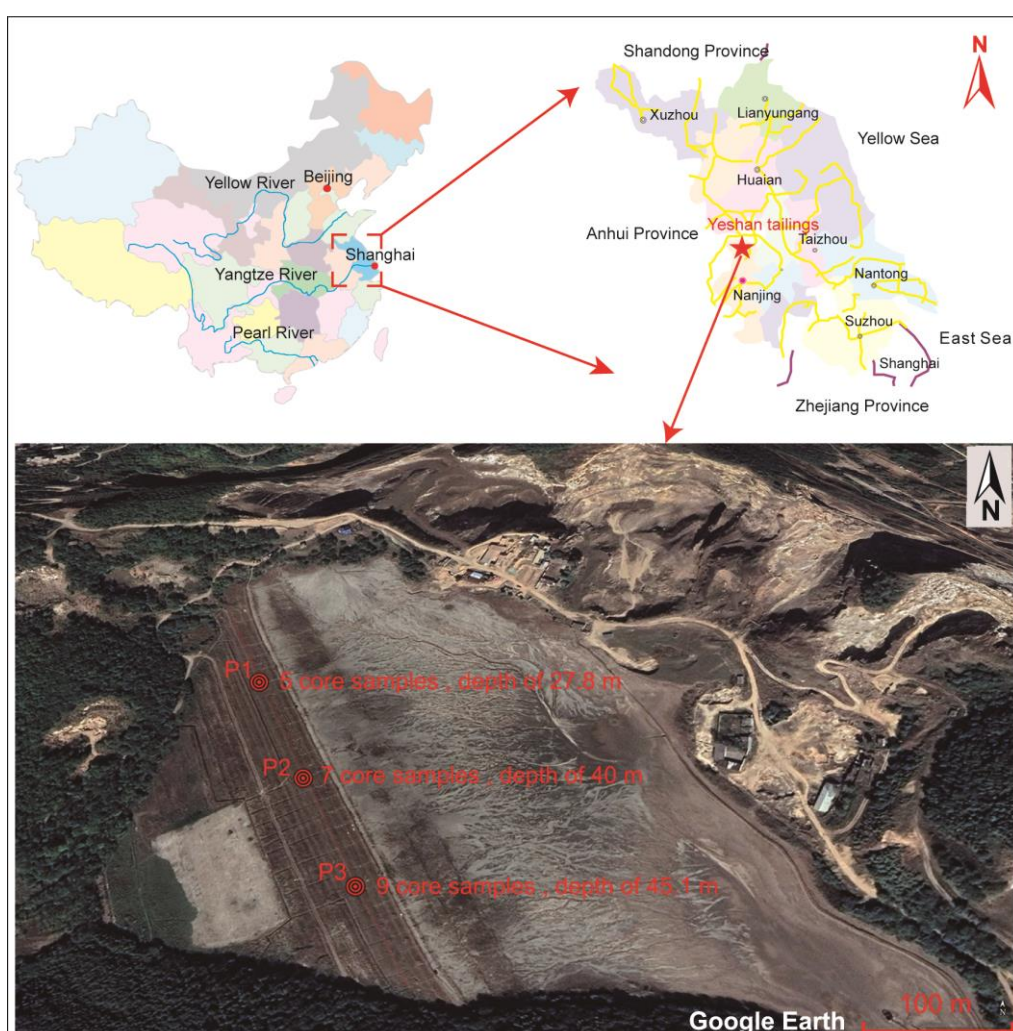


Fig. 1. Map showing the Yeshan iron tailings location and the sample collection sites in the tailings pond (image courtesy of Google Earth).

2.2. Sampling strategy

Core samples of tailings wastes were collected in-situ from three boreholes. As shown in Fig. 1, the sampling sites, P1, P2, and P3, were on a straight line and arranged along northwest to southeast transects. Elevation differences among the sampling sites were less than 0.6 m. With a drilling machine, core samples from each borehole were collected per 4 meters until the crushed rock layer. The detailed sampling information is listed in Table 1. The samples were collected to meet the following requirements of the study: (i) to cover the surface and bottom of the waste deposit; (ii) to collect sufficient samples for a statistical analysis of data. Altogether, twenty-one tailings samples, approximately 3.0 kg in weight, were obtained and transferred to the laboratory. All collected tailings samples were air-dried after homogenization. Lumps were broken apart and passed through a 2 mm sieve to eliminate gravels and roots of plants. Finally, each sample was sealed in a hermetic plastic bag with an identified number. Aliquots (ca. 300 g) of subsamples taken from each sample constituted the mixed sample.

Table 1

The detailed information for sampling in Yeshan iron tailings pond.

sampling site	Depth /m	Number of Samples	Description
P1	27.8	5	from 0 to 24 m, tailings; from 24 to 25 m, claypan; over 25 m, crushed rock.
P2	40	7	from 0 to 34.5 m, tailings; from 34.5 to 36.4 m, claypan; over 36.40 m crushed rock.
P3	45.1	9	from 0 to 35 m, tailings; from 35 to 41 m, claypan; over 41 m crushed rock.

2.4 Mineralogical analysis

Subsamples and the mixed sample were analyzed by X-ray diffraction using a Bruker AXS D8-Focus diffractometer with Cu K α radiation ($\lambda = 1.5406 \text{ \AA}$). X-ray diffraction data were collected between 5° and 60° with a step size of 0.02° . The crystalline phases were identified by matching peak positions of the intense peaks with those on PCPDF standard cards.

Based on scanning electron microscope (SEM) and energy dispersive spectrometer (EDS), the advanced mineral liberation analysis (MLA) system can provide detailed information about a wide variety of mineralogical characteristics, for instance, mineral identification, grain size distribution, mineral texture and association, and degree of mineral liberation²⁴. Therefore, the MLA technique is increasingly applied to analyses of tailings wastes mineralogical properties. MLA was performed

with SEM (Quanta 650, FEI, Netherlands), EDS (Quantax 200, Bruker, Germany) and mineral parameter automatic analysis software version 2.0.

2.5 Geochemical analysis

Quantitative analysis of the major elements was determined by X-ray fluorescence spectroscopy (XRF, Axios, Netherlands). A subset of each sample, with a mass of 10.0 g, was ground to a fraction less than 74 μm . A total of 8.0 g of each sample with 2.0 g of organic binder was further ground and homogenized using a mill. The organic binder consisted of 90 wt.% cellulose and 10 wt.% wax. Then, the mixtures were placed in an aluminum cup and pressed into pellets under a pressure of 15 MPa for 60 seconds. This step ensured sample integrity under vacuum and a consistent surface to receive the X-rays.

Inductively coupled plasma mass spectrometry (ICP-MS, Analytik Jena AG, PlasmaQuant MS) was applied to determine trace elements in the extracts. Briefly, 0.10 g of ground sample was placed in a clean 50 ml digestion tube and then digested with 8 ml aqua regia, a mixed solution of 96% HNO_3 and 36% HCl with a volume ratio of 1:1. The digestion process was performed at 140-160 °C until a white precipitate remained at the bottom of the tube. Then, the digested residuum was dissolved in 1% HNO_3 , and transferred to a volumetric flask and diluted to 50 ml. Blank sample values from mixed acids prepared in the same way were corrected for the measured data.

3. Results and Discussion

3.1. Mineralogical properties

The grain size distribution of mineralogical phases was evaluated from the scanning BSE images with the MLA system. As shown in Fig. 2, the proportions of individual minerals, including magnetite, limonite, siderite, pyrite, and chalcopyrite, were categorized with a distribution histogram for vol.%. The grain size distributions are similar in magnetite, limonite and siderite, which are concentrated in the < 20 μm population. Pyrite and chalcopyrite were the primary sulfide minerals that occurred with variable size fractions. Both were mainly concentrated in the 80~160 μm range, accounting for approximately 30 vol.%.

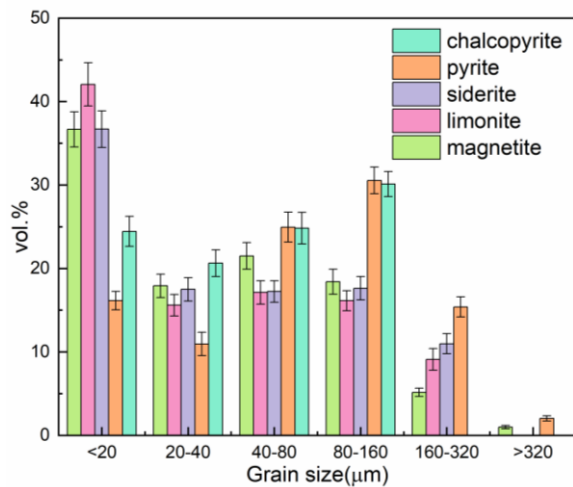


Fig. 2. Particle size distributions of mineralogical phases.

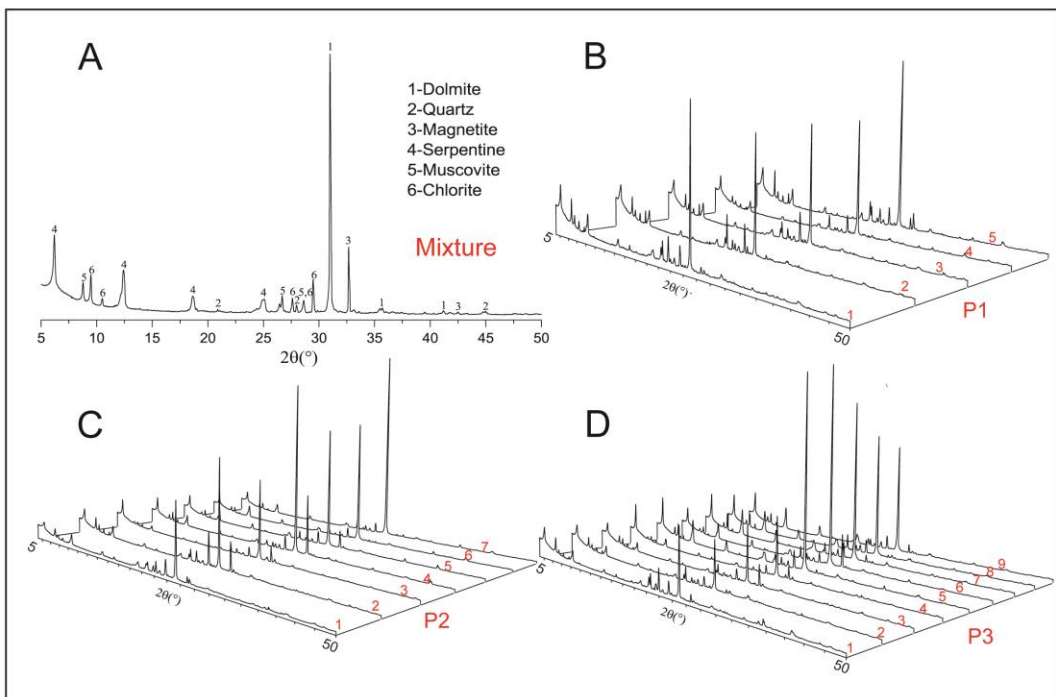


Fig. 3. X-ray diffraction patterns:(A) a typical XRD pattern of the mixture sample; (B) XRD patterns of 5 samples from borehole P1; (C) XRD patterns of 7 samples from borehole P2; (D) XRD patterns of 9 samples from borehole P3.

Fig. 3(A) shows a typical X-ray diffraction pattern of the mixed sample. Careful XRD investigation revealed that Yeshan IOTs consisted chiefly of dolomite, quartz, magnetite, muscovite, serpentine, and chlorite. The XRD patterns from borehole P1-P3 samples are shown in Fig.3 (B), (C), and (D), respectively. The diffraction peaks of the patterns were basically consistent, however, the significantly different intensities of diffraction peaks indicated the various contents of mineral phases in these samples. This phenomenon occurred not only in different sampling regions, but also at

different depths in the same borehole.

Table 2 Quantitative mineralogy of the mixed sample determined by the MLA system

Mineral	Ideal formula	Content/ wt.%
dolomite	$\text{CaMg}(\text{CO}_3)_2$	22.8 ± 1.1
serpentine	$\text{Mg}_6[\text{Si}_4\text{O}_{10}](\text{OH})_8$	16.9 ± 1.0
magnetite	Fe_3O_4	9.6 ± 0.9
quartz	SiO_2	8.7 ± 0.9
K-feldspar	KAlSi_3O_8	6.8 ± 0.7
chlorite	$(\text{Mg},\text{Fe})_5\text{Al}[\text{AlSi}_3\text{O}_{10}](\text{OH})_8$	6.2 ± 0.6
muscovite	$\text{KAl}_2[\text{AlSi}_3\text{O}_{10}](\text{OH})_2$	5.7 ± 0.6
diopside	$\text{Ca}_2\text{Mg}_5[\text{Si}_8\text{O}_{22}](\text{OH})_2$	4.8 ± 0.5
calcite	CaCO_3	4.1 ± 0.4
pyrite	FeS_2	3.3 ± 0.3
talc	$\text{Mg}_3[\text{Si}_4\text{O}_{10}](\text{OH})_2$	3.2 ± 0.3
siderite	FeCO_3	2.1 ± 0.2
limonite	$\text{FeO}(\text{OH})$	1.8 ± 0.2
epidote	$\text{Ca}_2\text{FeAl}_2[\text{Si}_2\text{O}_7][\text{SiO}_4]\text{O}(\text{OH})$	1.2 ± 0.1
ankerite	$\text{Ca}(\text{Fe},\text{Mg},\text{Mn})(\text{CO}_3)_2$	1.2 ± 0.1
magnesite	MgCO_3	0.8 ± 0.2
chalcopyrite	CuFeS_2	0.7 ± 0.2

As listed in Table 2, the mineral phases of mixed IOTs identified by the MLA system were consistent with the XRD results. However, some minor phases (e.g., K-feldspar, diopside, siderite, pyrite, etc.) were observed in thin sections because of the higher precision compared with XRD. After iron ore extraction, the magnetite content was still 9.6 ± 0.9 wt.%, while other iron-bearing minerals, such as pyrite, siderite and limonite, were also detected. The gangue minerals were dominated by dolomite and serpentine, which accounted for 22.8 ± 1.1 and 16.9 ± 1.0 wt.%, followed by quartz, K-feldspar and chlorite with contents of 8.7 ± 0.9 , 6.8 ± 0.7 , and 6.2 ± 0.6 wt.%, respectively. The proportions of muscovite, diopside, calcite, and talc ranged from 3.2 to 5.7 wt.%.

3.2 Mineral morphologies

The MLA system can provide valuable information on textural features of mineral assemblages on the micrometer scale. According to the gray values of BSE images, the intelligent software can identify individual phases based on an adequate mineral standard database²⁵. The BSE images with the automatic diagnoses of minerals given by the MLA system are shown in Fig. 4.

As presented in Fig. 4 (A), magnetite grains generally range from 10 to 200 μm in cross-section,

with a maximum of approximately 500 μm . Fine-grained and subhedral magnetite crystals were observed as occlusions with transparent minerals. At the same time, Fig. 4 (B) shows that the sectional coarse-grained magnetite crystals enfolded some gangue minerals. Multimineral intergrowths of pyrite with limonite, hematite and siderite were also observed. Fig. 4 (C) shows the complicated intergrowths of pyrite and limonite with crisscrossing grain boundaries. Fig. 4 (D) shows that irregular siderite aggregations occurred between hematite and pyrite. Fine-grained hematite possessing magnetite crystal shapes (Fig. 4 (E)), was enfolded by brucite. Chalcopyrite was observed in association with serpentine (Fig. 4 (F)). The investigation of mineral morphologies revealed that mineral liberation from tailings wastes was not completed and further grinding iron ore is necessary for higher recovery. Despite a few intergrowths existing in different minerals, the textural structures will allow easy liberation of the constituent mineral phases, suggesting the feasibility of recycling valuable metals from Yeshan IOTs.

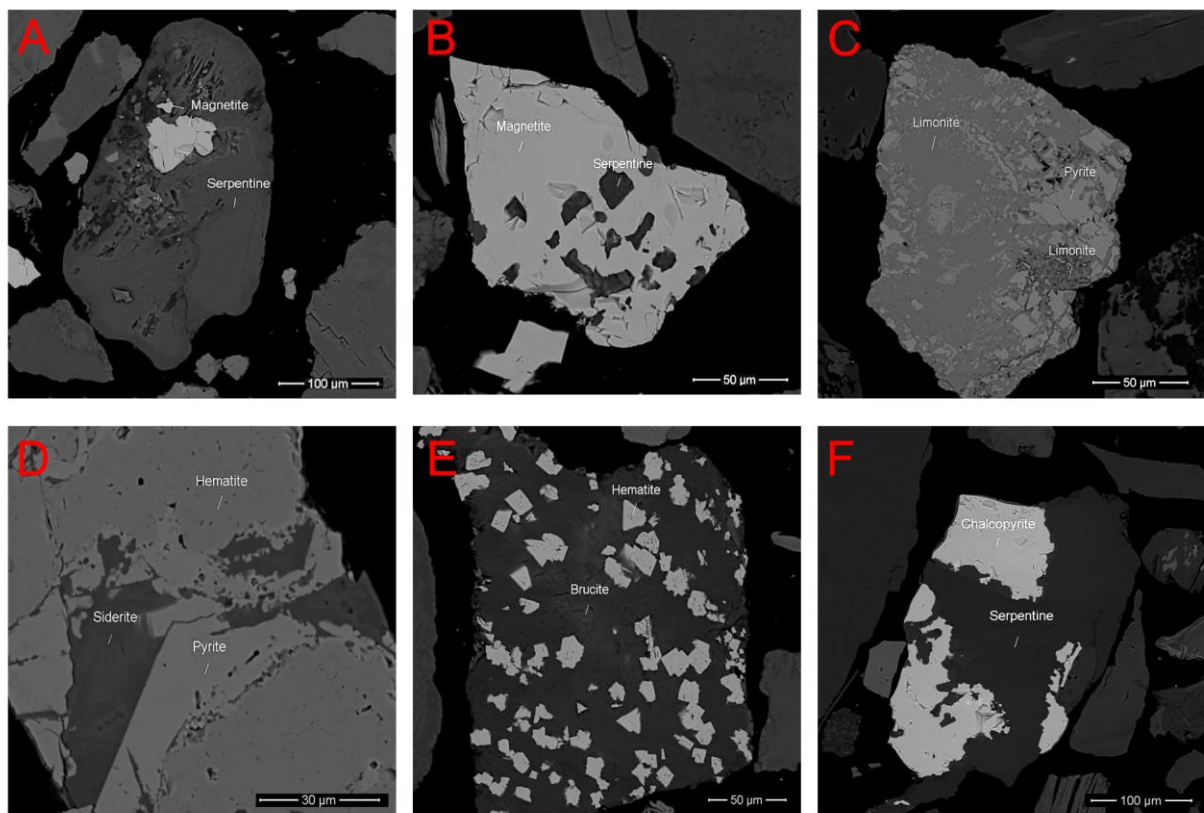


Fig. 4. BSE images from the MLA system: (A) magnetite is locked in serpentine; (B) serpentine is enriched in coarse-grained magnetite crystals; (C) complicated intergrowth of pyrite and limonite with crisscross grain boundaries; (D) irregular siderite aggregations occur between hematite and pyrite; (E) fine-grained hematite is enriched in brucite; (F) intergrowth of chalcopyrite and serpentine.

3.3. Geochemical characteristics

The major elements were investigated by XRF analysis, and the results are presented in Fig. 5. The occurrence of major elements from the measurements followed the order $\text{SiO}_2 > \text{TFe}_2\text{O}_3 > \text{MgO} > \text{CaO} > \text{Al}_2\text{O}_3 > \text{SO}_3 > \text{K}_2\text{O}$, where TFe_2O_3 denotes the total amount of iron oxide, including Fe_2O_3 and FeO . This order is basically consistent with the mineralogical characteristics, which indicated that dolomite, serpentine, magnetite, and quartz were the principal minerals. As shown in Fig. 6, four typical types of IOTs in China, are, high-silicon IOTs, high-alumina IOTs, high-calcium IOTs and high-magnesium IOTs, respectively. The percentage of MgO in Yeshan IOTs is much higher than that of high-magnesium IOTs, indicating that Yeshan IOTs are classified as high-magnesium IOTs. Small quantities of K_2O , Na_2O , P_2O_5 , TiO_2 and MnO were detected at levels less than 1 wt.%. The presence of K and Na cations could be ascribed to chlorite, K-feldspar and muscovite, while the phosphorus was presumably contributed by apatite. It is suspected that Ti substitutes for Al in aluminosilicate phases due to their similar atomic radii.

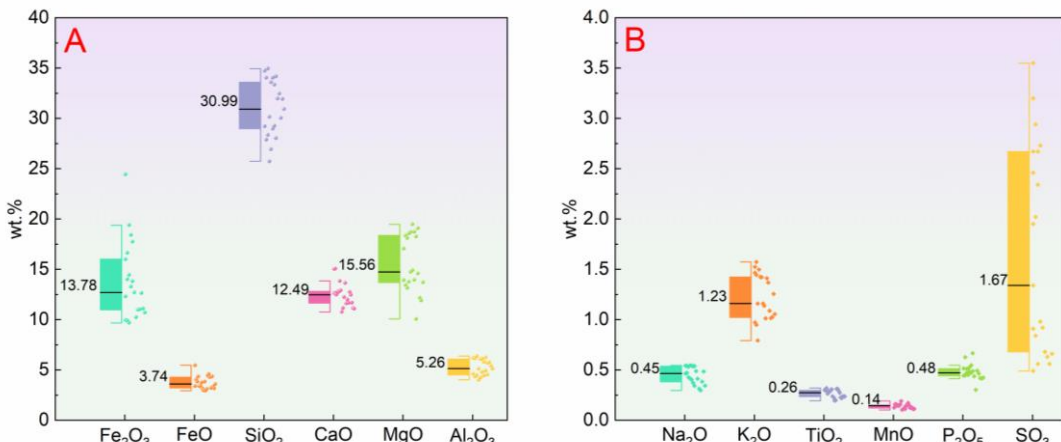


Fig. 5. Box and whisker plots for (A) major elements with contents more than 3 wt.% and (B) elements with contents less than 2 wt.%.

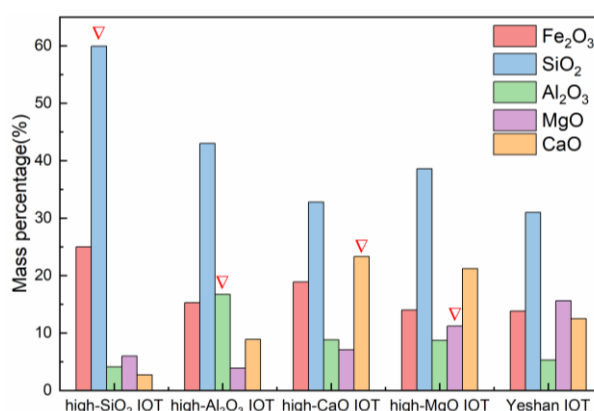


Fig. 6. Major components of Yeshan IOTs, compared with four typical types of IOTs in China.

A number of recent studies indicate that IOTs can be utilized as industrial raw materials to produce green and sustainable industrial products²⁶⁻³⁰. However, the extremely high content of MgO and high content of SO₃ in Yeshan IOTs could bring a huge challenge for using Yeshan IOTs as alternative raw meals to produce cement. It has been confirmed that abundant MgO and SO₃ in raw meals have negative effects on the formation of cement clinker^{31, 32}. Additionally, a large quantity of dolomite and serpentine, and relatively abundant clay minerals exist in Yeshan IOTs, which has adverse effects on the performance of concrete if the Yeshan IOTs replace natural fine aggregates in concrete. Therefore, using Yeshan IOTs sand for full aggregate replacement of natural gravel in cementitious materials could be impractical.

3.4. Spatial distribution

The changed composition of raw iron ore at different periods and frequent alterations of sand outlet positions can cause the elements to exhibit uneven spatial distributions. IOTs have been used as raw materials in construction building materials^{33, 34}, such as cement, concrete, non-burning bricks and ceramics. Figuring out the spatial distribution of major elements in tailings ponds is beneficial for more efficient and reasonable management and utilization of tailings. Ordinary Kriging^{35, 36} was applied to quantify the spatial variations of elements in the tailings pond. Enrichment locations of the elements can be determined visually and accurately with the support of a 2D vertical profile, which can provide essential information for exploiting Yeshan IOTs in the future.

Based on the chemical composition data at each sampling site, the spatial distribution maps are presented in Fig. 7. Here, the P1 site was defined as the ordinate origin, and the orientation of the x-axis was from P1 to P3. At the same time, Pearson correlation analysis was applied to preliminarily determine correlations between the concentrations of major elements. The positive correlation with highly significant correlations at $p < 0.01$ and $p < 0.05$ between elements indicates a similar original source

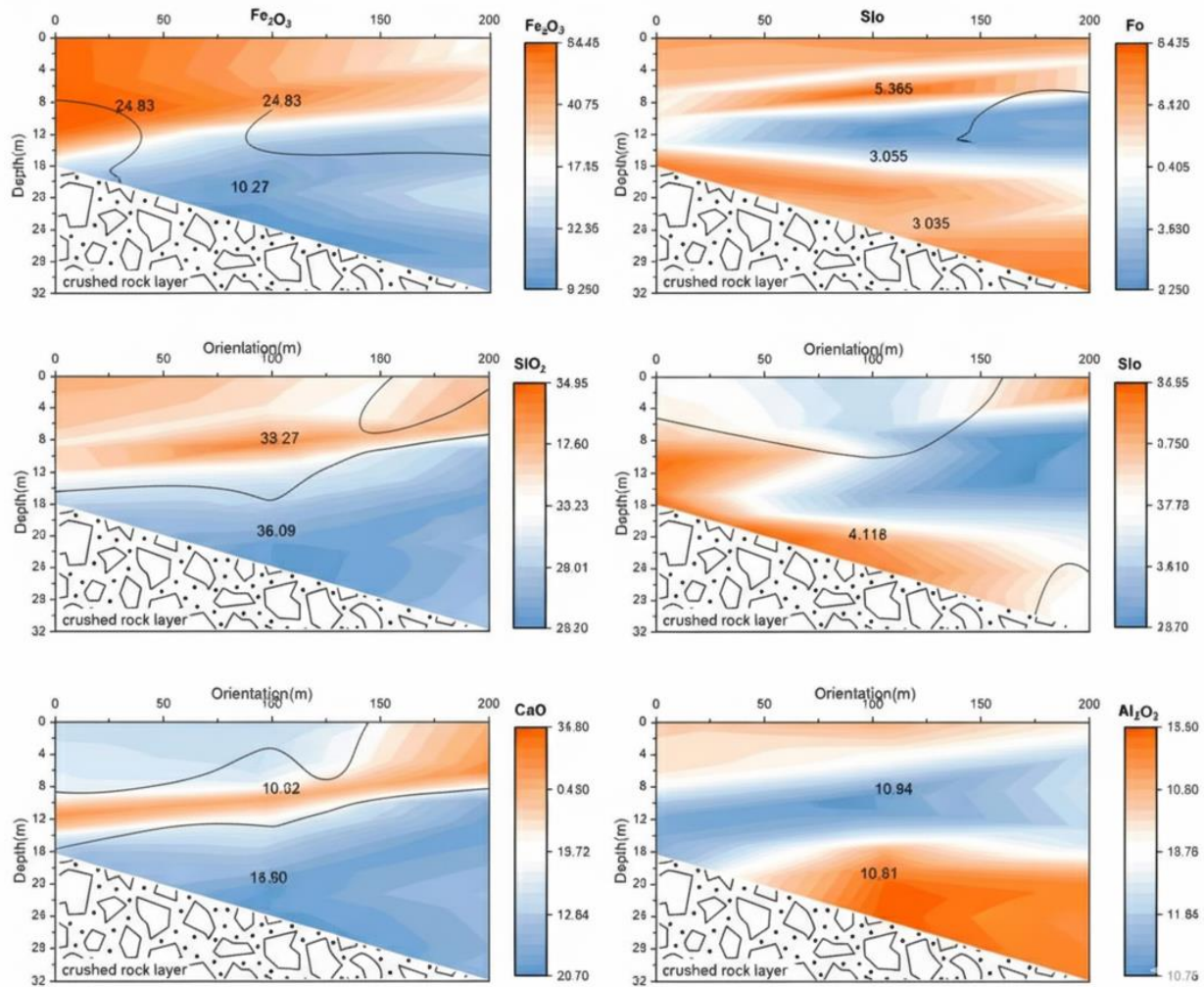


Fig. 7. Kriging maps of the spatial distribution of major elements in the vertical profile of the Yesan iron tailings pond.

The kriging maps clearly display that the major elements were distributed unevenly in the tailings pond. As shown in Fig. 7, the distributions of Fe_2O_3 and FeO are exactly the same, concentrating in the striped zonation at 6-10 m depth under the topsoil. The distribution of SiO_2 is consistent with Al_2O_3 , indicating that a large proportion of them come from the same aluminosilicate minerals. In Fig. 8, significant positive correlations between Fe_2O_3 and FeO ($r = 0.736, p < 0.01$), SiO_2 and Al_2O_3 ($r = 0.986, p < 0.01$), also suggest the possible same source of these elements. In addition, high contents of SiO_2 and Al_2O_3 were concentrated in the P1 region, and a low content of them were dispersed in the bottom layer of the P2 area. The highest concentrations of CaO occurred in the bottom layer of the P2 region, while, most MgO accumulated in the bottom layer of the P2 and P3 regions, and the accumulation region of MgO was obviously larger than that of CaO . MgO exhibited

significantly negative correlation with Fe_2O_3 ($r = -0.767, p < 0.01$), FeO ($r = -0.652, p < 0.01$), SiO_2 and Al_2O_3 (both $r = -0.548, p < 0.05$). Although part of CaO and MgO comes from the dolomite, the CaO distribution was slightly different from that of MgO . The heat map clearly showed that both MgO and CaO had highly negative correlations with Fe_2O_3 ($r = -0.767, p < 0.01$; $r = -0.570, p < 0.01$), however, MgO was weakly correlated with CaO .

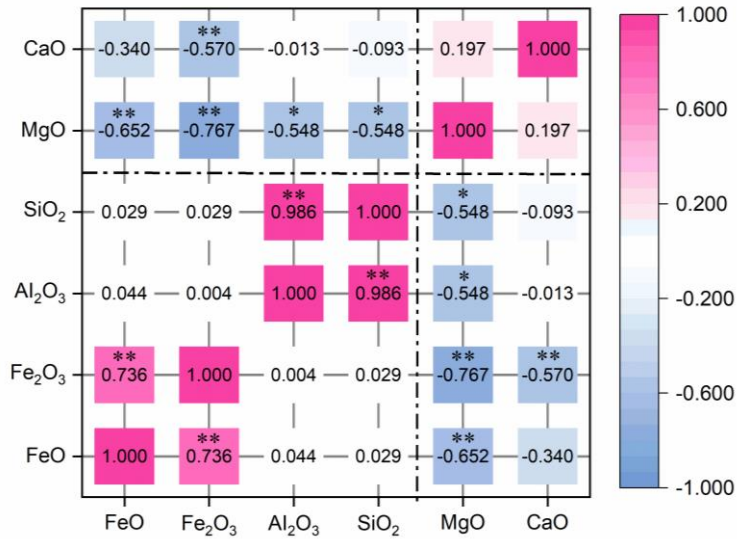


Fig. 8. Heat map of correlations between major elements based on Pearson correlation coefficients ($n=21$). The data is the r values. Blue, white, and red colors denote strong negative correlation, weak correlation, and strong positive correlation, respectively. “**” and “*” indicate significant correlations at $p < 0.01$ and $p < 0.05$, respectively.

4. Conclusion

The mineralogy and geochemistry of iron ore tailings from Yeshan iron deposit were investigated with an in-situ sampling approach, coupling mineralogical techniques, major element analysis, and visual technology. XRD and MLA analyses demonstrated that Yeshan IOTs primarily consisted of dolomite, serpentine, magnetite and quartz. The BSE images revealed the complex texture of IOTs and incomplete mineral liberation, indicating further grinding of iron ore is necessary for higher recovery and feasibility of recycling valuable metals from the IOTs. Owing to a great deal of dolomite, serpentine and clay, it could be impractical to replace natural gravel with Yeshan IOTs in concrete.

The major elements present in tailings wastes analyzed by XRF were SiO_2 , Fe_2O_3 , MgO and CaO . Due to high level of MgO , Yeshan IOTs were classified as high-magnesium IOTs. The abundant

MgO and SO₃ could cause great difficulty in applying Yeshan IOTs as raw cement meals. According to the 2D vertical distribution profiles created with the ordinary Kriging method, it is found that most of elements accumulated in certain strata and the variation trends were inconsistent. Fe₂O₃ and FeO, SiO₂ and Al₂O₃, showed significant positive correlations, while MgO exhibited a weak correlation with CaO. The 2D vertical element distribution profiles can provide visual information about the elements for exploiting Yeshan IOTs.

Author Contribution statement

G. Yang: Methodology, Formal analysis, Data curation, Writing - original draft, Writing - review & editing; **Quanmin Xie:** Resources, Coordination; **Yidi Li:** Formal analysis, Data curation; **E. Ranjith Kumar:** Review & editing; **Fang Liu:** Investigation, Conceptualization, Coordination; **Mei Yang:** Methodology, Resources, Review.

Declaration of competing interest

The authors declare that they have no known competing financial interests or personal relationships that could have appeared to influence the work reported in this paper.

Data availability

Data is uploaded as Supporting for Information only.

Acknowledgements

The authors thank Yeshan Mining Co., Ltd. and Wuhan Explosion and Blasting Co., Ltd. for supporting this work. The authors also would like to express their appreciation to the anonymous reviewer for some constructive suggestions.

References

1. Nishijima, M.; Rocha, F. F. An economic investigation of the dengue incidence as a result of a tailings dam accident in Brazil. *J. Environ. Manag.* 2020, 253, 109748.
2. Wang, J.; Liu, J.; Li, D.; Chen, C.; Cheng, J. Geochemical distribution and mineralogy of heavy metals in the gasification residue of coal-waste activated carbon-slurry: Insights into leaching behavior. *J. Hazard. Mater.* 2023, 451, 131146.
3. Kossoff, D.; Dubbin, W. E.; Alfredsson, M.; Edwards, S. J.; Macklin, M. G.; Hudson-Edwards, K. A. Mine tailings dams: Characteristics, failure, environmental impacts, and remediation. *Appl. Geochem.* 2014, 51, 229–245.
4. Zhao, J.; Ni, K.; Su, Y.; Shi, Y. An evaluation of iron ore tailings characteristics and iron ore tailings concrete properties. *Constr. Build. Mater.* 2021, 286, 122968.
5. Kobayashi, H.; Garnier, J.; Mulholland, D. S.; Quantin, C.; Haurine, F.; Tonha, M.; Joko, C.; Olivetti, D.; Freydier,

- R.; Seyler, P.; Martinez, J.-M.; Roig, H. L. Exploring a new approach for assessing the fate and behavior of the tailings released by the Brumadinho dam collapse (Minas Gerais, Brazil). *J. Hazard. Mater.* 2023, 448, 130828.
6. Young, G.; Yang, M. Preparation and characterization of Portland cement clinker from iron ore tailings. *Constr. Build. Mater.* 2019, 197, 152-156.
7. Pan, H.; Zhou, G.; Cheng, Z.; Yang, R.; He, L.; Zeng, D.; Sun, B. Advances in geochemical survey of mine tailings project in China. *J. Geochem. Explor.* 2014, 139, 193-200.
8. Wu, S.; Liu, Y.; Southam, G.; Robertson, L.; Chiu, T. H.; Cross, A. T.; Dixon, K. W.; Stevens, J. C.; Zhong, H.; Chan, T.-S.; Lu, Y.-J.; Huang, L. Geochemical and mineralogical constraints in iron ore tailings limit soil formation for direct phytostabilization. *Sci. Total Environ.* 2019, 651, 192-202.
9. Achillas, C.; Moussiopoulos, N.; Karagiannidis, A.; Banias, G.; Perkoulidis, G. The use of multi-criteria decision analysis to tackle waste management problems: a literature review. *Waste Manag. Res.* 2013, 31, 115-129.
10. Jamieson, H. E.; Walker, S. R.; Parsons, M. B. Mineralogical characterization of mine waste. *Appl. Geochem.* 2015, 57, 85-105.
11. Rey, V.; Ríos, C. A.; Vargas, L. Y.; Valente, T. M. Use of natural zeolite-rich tuff and siliceous sand for mine water treatment from abandoned gold mine tailings. *J. Geochem. Explor.* 2021, 220, 106660.
12. Queiroz, H. M.; Ruiz, F.; Deng, Y.; de Souza Júnior, V. S.; Ferreira, A. D.; Otero, X. L.; de Lima Camêlo, D.; Bernardino, A. F.; Ferreira, T. O. Mine tailings in a redox-active environment: Iron geochemistry and potential environmental consequences. *Sci. Total Environ.* 2022, 807, 151050.
13. Lemos, M.; Valente, T.; Reis, P. M.; Fonseca, R.; Pantaleão, J. P.; Guabiroba, F.; Filho, J. G.; Magalhães, M.; Afonso, B.; Silva, A. R.; Delbem, I. Geochemistry and mineralogy of auriferous tailings deposits and their potential for reuse in Nova Lima Region, Brazil. *Scientific Reports* 2023, 13, 4339.
14. Zhang, A.; Bain, J. G.; Schmall, A.; Ptacek, C. J.; Blowes, D. W. Geochemistry and mineralogy of legacy tailings under a composite cover. *Appl. Geochem.* 2023, 159, 105819.
15. Ma, B.-g.; Cai, L.-x.; Li, X.-g.; Jian, S.-w. Utilization of iron tailings as substitute in autoclaved aerated concrete: physico-mechanical and microstructure of hydration products. *J. Clean. Prod.* 2016, 127, 162-171.
16. Li, X.; Zhang, N.; Yuan, J.; Wang, X.; Zhang, Y.; Chen, F.; Zhang, Y. Preparation and microstructural characterization of a novel 3D printable building material composed of copper tailings and iron tailings. *Constr. Build. Mater.* 2020, 249, 118779.
17. Li, L.; Jiang, T.; Chen, B.; Zhou, M.; Chen, C. Overall utilization of vanadium–titanium magnetite tailings to prepare lightweight foam ceramics. *Process Saf. Environ. Prot.* 2020, 139, 305-314.
18. Liu, T.; Lin, C.; Liu, J.; Han, L.; Gui, H.; Li, C.; Zhou, X.; Tang, H.; Yang, Q.; Lu, A. Phase evolution, pore morphology and microstructure of glass ceramic foams derived from tailings wastes. *Ceram. Int.* 2018, 44, 14393-14400.
19. Xie, L.; van Zyl, D. Distinguishing reclamation, revegetation and phytoremediation, and the importance of geochemical processes in the reclamation of sulfidic mine tailings: A review. *Chemosphere* 2020, 252, 126446.
20. García-Carmona, M.; García-Robles, H.; Turpín Torrano, C.; Fernández Ondoño, E.; Lorite Moreno, J.; Sierra Aragón, M.; Martín Peinado, F. J. Residual pollution and vegetation distribution in amended soils 20 years after a pyrite mine tailings spill (Aznalcóllar, Spain). *Sci. Total Environ.* 2019, 650, 933-940.
21. Simonsen, A. M. T.; Solismaa, S.; Hansen, H. K.; Jensen, P. E. Evaluation of mine tailings' potential as supplementary cementitious materials based on chemical, mineralogical and physical characteristics. *Waste Manag.* 2020, 102, 710-721.
22. Vaziri, V.; Sayadi, A. R.; Parbhakar-Fox, A.; Mousavi, A.; Monjezi, M. Improved mine waste dump planning through integration of geochemical and mineralogical data and mixed integer programming: Reducing acid rock generation from mine waste. *J. Environ. Manag.* 2022, 309, 114712.
23. Du, P.; Chen, J.; Bai, X.; Han, W. Understanding the seasonal variations of land surface temperature in Nanjing

- urban area based on local climate zone. *Urban Clim.* 2020, 33, 100657.
24. Fandrich, R.; Gu, Y.; Burrows, D.; Moeller, K. Modern SEM-based mineral liberation analysis. *Int. J. Miner. Process.* 2007, 84, 310–320.
25. Redwan, M.; Rammlmair, D.; Meima, J. A. Application of mineral liberation analysis in studying micro-sedimentological structures within sulfide mine tailings and their effect on hardpan formation. *Science of The Total Environment* 2012, 414, 480–493.
26. Li, N.; Lv, S.; Wang, W.; Guo, J.; Jiang, P.; Liu, Y. Experimental investigations on the mechanical behavior of iron tailings powder with compound admixture of cement and nano-clay. *Constr. Build. Mater.* 2020, 254, 119259.
27. Li, C.; Sun, H.; Yi, Z.; Li, L. Innovative methodology for comprehensive utilization of iron ore tailings: Part 2: The residues after iron recovery from iron ore tailings to prepare cementitious material. *J. Hazard. Mater.* 2010, 174, 78–83.
28. Luo, L.; Zhang, Y.; Bao, S.; Chen, T. Utilization of Iron Ore Tailings as Raw Material for Portland Cement Clinker Production. *Advances in Materials Science and Engineering* 2016, 2016, 1596047.
29. Han, X.; Wang, Y.; Zhang, N.; Meng, J.; Li, Y.; Liang, J. Facile synthesis of mesoporous silica derived from iron ore tailings for efficient adsorption of methylene blue. *Colloids and Surfaces A: Physicochemical and Engineering Aspects* 2021, 617, 126391.
30. Han, X.; Wang, F.; Zhao, Y.; Meng, J.; Tian, G.; Wang, L.; Liang, J. Recycling of iron ore tailings into magnetic nanoparticles and nanoporous materials for the remediation of water, air and soil: a review. *Environ. Chem. Lett.* 2023, 21, 1005–1028.
31. Li, X.; Huang, H.; Xu, J.; Ma, S.; Shen, X. Statistical research on phase formation and modification of alite polymorphs in cement clinker with SO₃ and MgO. *Constr. Build. Mater.* 2012, 37, 548–555.
32. Staněk; Theodor. The Influence of SO₃ and MgO on Kinetics of Alite Formation. *Procedia Engineering* 2016, 151, 26–33.
33. Vilela, A. P.; Eugênio, T. M. C.; de Oliveira, F. F.; Mendes, J. F.; Ribeiro, A. G. C.; Brandão Vaz, L. E. V. d. S.; Mendes, R. F. Technological properties of soil-cement bricks produced with iron ore mining waste. *Constr. Build. Mater.* 2020, 262, 120883.
34. Veiga Simão, F.; Chambart, H.; Vandemeulebroeke, L.; Nielsen, P.; Adrianto, L. R.; Pfister, S.; Cappuyns, V. Mine waste as a sustainable resource for facing bricks. *J. Clean. Prod.* 2022, 368, 133118.
35. Liu, L.; Liu, Q.; Ma, J.; Wu, H.; Qu, Y.; Gong, Y.; Yang, S.; An, Y.; Zhou, Y. Heavy metal(lloid)s in the topsoil of urban parks in Beijing, China: Concentrations, potential sources, and risk assessment. *Environ. Pollut.* 2020, 260, 114083.
36. Yuan, Y.; Xiang, M.; Liu, C.; Theng, B. K. G. Geochemical characteristics of heavy metal contamination induced by a sudden wastewater discharge from a smelter. *J. Geochem. Explor.* 2017, 176, 33–41.